Atmos. Chem. Phys., 26, 2769–2784, 2026
https://doi.org/10.5194/acp-26-2769-2026

Atmospheric Chemistry and Physics
Open Access
EGU

Research article

Process-level simulation of chemical composition, size distribution and cloud condensation nuclei of secondary organic aerosol from α-pinene ozonolysis

Zhen Song[1,2,3,4], Chenqi Zhang[1], Hongru Shen[1,a], Hao Ma[1], Iida Pullinen[6,b], and Defeng Zhao[1,3,4,5]

[1]Department of Atmospheric and Oceanic Sciences & Institute of Atmospheric Sciences, Fudan University, Shanghai, China
[2]Shanghai Frontiers Science Center of Atmosphere-Ocean Interaction, Fudan University, Shanghai, 200438, China
[3]Shanghai Key Laboratory of Ocean-land-atmosphere Boundary Dynamics and Climate Change, Fudan University, Shanghai, 200438, China
[4]National Observations and Research Station for Wetland Ecosystems of the Yangtze Estuary, Fudan University, Shanghai, 200438, China
[5]Institute of Eco-Chongming (IEC), 1050 Baozhen, Lühua Town, Chongming District, Shanghai 202151, China
[6]Institute of Energy and Climate Research, IEK-8: Troposphere, Forschungszentrum Jülich, Jülich, Germany
[a]present address: School of Environmental Science and Engineering, Shanghai Jiao Tong University, Shanghai 200240, PR China
[b]present address: Department of Technical Physics, University of Eastern Finland, Kuopio, 70211, Finland

Correspondence: Defeng Zhao (dfzhao@fudan.edu.cn)

Received: 8 September 2025 – Discussion started: 30 September 2025
Revised: 7 January 2026 – Accepted: 9 February 2026 – Published: 24 February 2026

Abstract. Secondary organic aerosols (SOA) contribute significantly to cloud condensation nuclei (CCN), which depend on particle size distribution (PSD), chemical composition and the hygroscopicity parameter (κ). Simulating SOA and CCN in chemical transport models relies on parameterizations, which need to be evaluated and improved against process-level models as a benchmark. Here, we simulated SOA concentration, chemical composition, PSD, κ, and CCN in α-pinene ozonolysis, a classical system for SOA studies, using a process-level box model PyCHAM with near-explicit chemical mechanisms. We assessed how CCN, chemical composition, PSD and κ can be modelled against measurements and evaluated the influence of these factors on CCN simulation. The model well simulated SOA mass concentration but overestimated O : C and H : C ratios, suggesting a possible lack of particle-phase chemistry. Highly oxygenated molecules (HOMs) contributed substantially to SOA mass. Simulated κ closely agreed with measurements at moderate supersaturation (0.37 %) but was overestimated at low supersaturation (0.19 %) and underestimated at high supersaturation (0.55 % and 0.73 %). Particle growth and number concentrations were reasonably reproduced, though the simulated PSD was broader and flatter than measurement. Simulated CCN concentrations agreed well with measurements at moderate to high supersaturation (0.37 %–0.73 %) but were overestimated at low supersaturation (0.19 %). Sensitivity analysis highlights the importance of accurately representing both PSD and κ for reliable CCN prediction, especially at supersaturation < 0.4 %. This study also highlights that HOM formation, finer PSD resolution and improved κ parameterizations are warranted in future chemical transport models, and evaluates the ability and limitations of this benchmark model.

Published by Copernicus Publications on behalf of the European Geosciences Union.

1 Introduction

Secondary organic aerosol (SOA), formed through the oxidation of volatile organic compounds (VOCs) and gas-particle partitioning, constitutes a significant fraction of atmospheric submicron aerosol mass (Jimenez et al., 2009; Huang et al., 2014; Shrivastava et al., 2017). As a result, SOA contributes significantly to global cloud condensation nuclei (CCN), influencing aerosol indirect effects (aerosol-cloud interaction) and radiative forcing (IPCC, 2021).

Despite numerous research efforts, uncertainties persist in assessing indirect effects of SOA on climate. These uncertainties are closely linked to inaccuracies in simulated CCN number concentrations within chemical transport models (IPCC, 2021). The contribution of SOA to CCN concentrations depends on the SOA concentration (Liu and Wang, 2010; Mei et al., 2013) and CCN activity of SOA, which is determined by their particle size distribution (PSD) and hygroscopicity (Farmer et al., 2015; Seinfeld and Pandis, 2016). Therefore, uncertainties in modeled CCN levels are strongly influenced by these parameters (McFiggans et al., 2006). In current chemical transport models, to enhance computational efficiency and numerical stability, SOA and CCN formation relies on simplified parameterizations which have been developed and optimized based on laboratory measurements or ambient data (Hodzic and Jimenez, 2011). For example, lumped species and reactions are usually adopted for gas-phase chemical mechanisms. Limited aerosol size bin resolution is typically used to represent size distribution and number concentration (Kanakidou et al., 2005; Yu and Luo, 2009; Luo and Yu, 2011; Topping and Bane, 2022). The volatility bases set (VBS) and its derivatives are often used to represent chemical composition of SOA via gas-particle partitioning (Donahue et al., 2006). Moreover, the hygroscopicity parameter (κ), derived from Köhler theory (Petters and Kreidenweis, 2007), is parameterized either as a uniform value for organic aerosols (OA) in most global models (Fanourgakis et al., 2019) or as several constant values for different OA types in regional models (Wang et al., 2019; Kuang et al., 2020). While these parameterizations or simplifications provide useful and efficient approaches to model SOA composition, concentrations, and CCN concentrations, it is necessary to evaluate them against process-level models as a benchmark. Such process-level models can provide a mechanistic representation of SOA chemistry and corresponding CCN formation by incorporating explicit or near-explicit chemical mechanisms and physicochemical processes such as detailed chemistry, gas-particle partitioning, fine particle size bin, and explicit treatment of κ. Such models are suitable for simulating SOA and CCN in chamber or laboratory studies and for developing more detailed bottom-up parameterizations applicable to chemical transport models. Moreover, such models can be used to improve chemical transport models, potentially through training artificial intelligence (AI)-based models capable of learning detailed parameterizations (Xia et al., 2025). In addition, this process-level approach enables the assessment of factors controlling SOA-derived CCN based on explicit chemical composition (which determines κ) and PSD simulations.

Over the past two decades, based on comprehensive explicit or near-explicit gas-phase chemical mechanisms, numerous studies have modeled SOA formation by oxidation of biogenic VOCs (Jenkin, 2004; Xia et al., 2008; Capouet et al., 2008; Ceulemans et al., 2010; Chen et al., 2011; Valorso et al., 2011; Zuend and Seinfeld, 2012; Gatzsche et al., 2017; Galeazzo et al., 2021) or anthropogenic VOCs (Johnson et al., 2004, 2005; Hu et al., 2007; Camredon et al., 2007; Kelly et al., 2010; Xu, 2014; La et al., 2016; Lannuque et al., 2023) under different conditions in chamber environment. The MCM (Master Chemical Mechanism), comprising 143 VOCs species and approximately 17 000 reactions, is the most widely used near-explicit mechanism (Jenkin et al., 1997, 2003; Saunders et al., 2003). Similar near-explicit or explicit chemical mechanisms include CACM (Caltech Atmosphere Chemistry Mechanism) (Griffin et al., 2002), GECKO-A (Generator for Explicit Chemistry and Kinetics of Organics in the Atmosphere) (Aumont et al., 2005; Camredon et al., 2007), PRAM (Peroxy Radical Autoxidation Mechanism) for the production of gas-phase Highly Oxygenated organic Molecules (HOMs) (Roldin et al., 2019), and other diversified VOCs oxidation mechanisms constructed by different studies (Peeters et al., 2001; Capouet et al., 2004, 2008; Hu et al., 2007; Ceulemans et al., 2010). HOMs, a group of VOC oxidation products formed through rapid autoxidation, play a critical role in SOA formation due to their low volatility and high oxygen content (Ehn et al., 2014; Bianchi et al., 2019). Modeling studies have demonstrated the importance of HOMs in SOA production from α-pinene and Δ^3-carene ozonolysis reactions (Roldin et al., 2019; Xu, 2021; Luo et al., 2024; Thomsen et al., 2024). In the models simulating SOA formation, gas-particle partitioning has been modeled based on thermodynamic absorption equilibrium partitioning theory (Pankow, 1994) or dynamic gas-particle mass transfer partitioning (Seinfeld and Pandis, 2016). Besides gas-phase reaction and gas-particle partitioning, particle-phase reactions, such as oligomerization and polymerization, have also been shown to affect SOA composition in the model simulation, although their importance varies across environmental conditions and reaction systems (Jenkin, 2004; Johnson et al., 2004, 2005; Xu, 2014; Hu et al., 2007; Chen et al., 2011; Galeazzo et al., 2021; Jia and Xu, 2021; Zhao et al., 2023; Lopez et al., 2025). Additionally, model studies have also discussed the influence of non-ideality mixing and vapor pressure estimation methods on SOA simulations (Ceulemans et al., 2010; Kelly et al., 2010; Valorso et al., 2011; Zuend and Seinfeld, 2012).

Despite advancements in chemical mechanisms and gas-particle partitioning models, SOA simulations still exhibit limitations. Most SOA modeling studies focus on SOA mass concentrations or yields, whereas far fewer have sim-

ulated chemical composition, PSD and CCN concentrations (Jenkin, 2004; Johnson et al., 2004, 2005; Hu et al., 2007; Xia et al., 2008; Capouet et al., 2008; Chen et al., 2011; Xu, 2014). Simulated chemical composition often shows substantial discrepancies relative to measurements. For example, the average oxygen-to-carbon ratio (O : C) and hydrogen-to-carbon ratio (H : C) of simulated SOA showed significant gaps compared with measured SOA in different VOCs oxidation reactions (Chen et al., 2011). Roldin et al. (2019) reproduces SOA mass from α-pinene ozonolysis based on reasonable HOM simulation but overestimates H : C, while O : C shows smaller bias at the average level. Pichelstorfer et al. (2024) captures the mass distribution of gas-phase HOMs and the monomer/dimer ratio, and achieves good agreement with SOA yield under low-NO_x conditions, but underestimates SOA formation under high-NO_x conditions. Moreover, few studies have simulated the particle size, which is crucial to SOA physical properties. Jia and Xu (2021) developed the CSVA (Core-Shell box model for Viscosity dependent SOA) model to simulate PSD evolution considering viscosity effects. O'Meara et al. (2021) developed the PyCHAM box model (CHemistry with Aerosol Microphysics in Python), which includes aerosol microphysics and can simulate PSD. Xu (2021) used PyCHAM to simulate PSD evolution of SOA from α-pinene ozonolysis, capturing overall growth but with a delayed peak compared to measurement. To date, simulation of SOA hygroscopicity and CCN number concentrations using near-explicit chemical mechanisms remain limited.

In this study, we simulated the concentration and chemical composition of SOA formed from α-pinene ozonolysis, a benchmark system in SOA studies, and CCN concentrations using PyCHAM model. Simulated SOA mass, number concentrations, chemical composition, size distribution, κ, and CCN number concentrations were evaluated against measurements. We further investigated the impact of SOA κ and PSD representation on CCN. This study aims to evaluate the capability and limitations of process-level modeling of SOA concentrations, chemical composition, PSD, and CCN using a bottom-up approach as a potential benchmark model. In the future, once validated and improved such a benchmark model for SOA and CCN simulation can be used for assessing SOA and CCN parameterizations in chemical transport models and may be used to improve chemical transport models, potentially through training AI-based models capable of learning detailed parameterizations.

2 Methods

2.1 SAPHIR chamber and experiment

The α-pinene ozonolysis experiment was conducted in the SAPHIR (Simulation of Atmospheric PHotochemistry In a large Reaction) chamber at Forschungszentrum Jülich, Germany. SAPHIR is a 270 m^3 double-walled cylindrical Teflon chamber with a surface-to-volume ratio of $\sim 1\ m^2\ m^{-3}$, as previously described (Rohrer et al., 2005; Zhao et al., 2015). The chamber utilizes natural sunlight for illumination and features a louvre system to switch between light and dark conditions. For this study, the experiment was performed in the dark with the louvres closed. Prior to the experiment, the chamber was flushed with high-purity synthetic air (purity $> 99.9999\ \%$ O_2 and N_2). The experiment was conducted at a relative humidity (RH) of 37 %–79 % and a temperature range of 291.2–299.1 K (Fig. S1 in the Supplement). A total of 20 ppbv of α-pinene was introduced into the chamber, followed by the addition of 50 ppbv O_3 after 30 min to initiate organic chemistry. The experiment lasted approximately 8.5 h, and no seed aerosols were used.

Temperature and RH were monitored continuously throughout the experiment. A scanning mobility particle sizer (SMPS, TSI DMA3081/TSI CPC3785) measured SOA mass and number concentrations and size distributions over the range 9.82–429.4 nm. A cloud condensation nuclei counter (CCN100, Droplet Measurement Technique, USA) measured CCN number concentrations at four supersaturations (SS): 0.19 %, 0.37 %, 0.55 %, and 0.73 %. Based on parallel measurements of CCN and total particle number (cloud nuclei; CN) for each size bin in a continuous flow, the critical activation particle size (D_{crit}) at each SS was determined using the Scanning Mobility CCN Analysis (SMCA) method (Moore et al., 2010; Zhao et al., 2015, 2016). Briefly, CN and CCN concentrations for each size bin were used to calculate the CCN activation fraction (CCN / CN). Before computing CCN / CN, the measured CCN and CN concentrations were corrected for multiple charged particles. Then, CCN / CN for each charge class was then fitted using a Gaussian error function, and the turning point of this function was taken as D_{crit} at the specific SS. For each SS, at least three full scans were performed, and the resulting D_{crit} were averaged. The SS calibration followed Zhao et al. (2016) and Zhang et al. (2023). Then κ parameter at four SS was derived from κ–Köhler equation given different SS and corresponding D_{crit} (Petters and Kreidenweis, 2007). The error bars for κ were estimated from the standard deviation of D_{crit} across three duplicate scans. A high-resolution time-of-flight aerosol mass spectrometer (HR-ToF-AMS, Aerodyne Research Inc., DeCarlo et al., 2006) provided SOA chemical composition data, including O : C and H : C elemental ratios. O_3 concentrations were measured using a UV photometer O_3 analyzer (ANSYCO, model O341M). OH, HO_2, and RO_2 radical concentrations were quantified using a home-built laser-induced fluorescence system (LIF) (Fuchs et al., 2012). VOCs were measured using a proton transfer reaction time-of-flight mass spectrometer (PTR-ToF-MS, Ionicon Analytik, Austria). Gas-phase oxygenated organic molecules (OOMs) participating in gas-particle partitioning, including HOMs, were measured using a chemical ionization atmospheric pressure interface time-of-flight mass spectrom-

eter (CIMS, Tofwerk AG/Aerodyne Research, Inc.) with nitrate (NO_3^-) as the reagent ion (NO_3^--CIMS).

2.2 PyCHAM box modeling

The α-pinene ozonolysis experiment was simulated using the PyCHAM (CHemistry with Aerosol Microphysics in Python) model (v5.5.9) (O'Meara et al., 2021). PyCHAM was developed with two precursor models as platforms: the Microphysical Aerosol Numerical model Incorporating Chemistry (MANIC) for multiphase processes (Lowe et al., 2009) and PyBox for Python-based parsing and automatic generation of chemical reaction modules (Topping et al., 2018). PyCHAM is designed to simulate aerosol chamber experiments, enabling comparisons between simulations and observations to improve process understanding for atmospheric applications.

PyCHAM solves coupled ordinary differential equations for gas-phase chemistry, gas-particle partitioning, and gas-wall partitioning following Jacobson (2005). Gas–particle partitioning follows the formulation of Zaveri et al. (2008):

$$\frac{\mathrm{d}C_{i,\mathrm{g}}}{\mathrm{d}t} = -\sum_{j=1}^{N} k_{i,j}\left(C_{i,\mathrm{g}} - x_{i,j}\,p_i^0 K_{v,j}\gamma_{i,j}\right), \quad (1)$$

$$\frac{\mathrm{d}C_{i,j}}{\mathrm{d}t} = k_{i,j}\left(C_{i,\mathrm{g}} - x_{i,j}\,p_i^0 K_{v,j}\gamma_{i,j}\right), \quad (2)$$

where component i partitions into size bin j from the gas phase g, with N total size bins. Here, x is the particle-phase mole fraction, p^0 is the pure component liquid (sub-cooled if necessary) vapour pressure, K_v is the Kelvin factor and γ is the activity coefficient. Because no well-established data of γ were available for our experimental conditions, we only simulated the idealized conditions (i.e. γ for all components were set to 1). The first-order mass transfer coefficient $k_{i,j}$ for component i to size bin j incorporates the Fuchs-Sutugin transition regime correction (Fuchs and Sutugin, 1971) and can be adjusted based on mass accommodation coefficient (α_i) of individual component:

$$k_{i,j} = 4\pi\overline{R_{\mathrm{p},j}}D_{\mathrm{g},i}N_j f\left(Kn_{i,j},\alpha_i\right), \quad (3)$$

where $\overline{R}_{\mathrm{p},j}$ (cm) is mean wet radius of particles in bin j; $D_{\mathrm{g},i}$ ($\mathrm{cm^2\,s^{-1}}$) is gas diffusivity of species i; N_j ($\mathrm{cm^{-3}}$) is the number concentration of particles in bin j; α_i means the chance that component i can stick to a particle surface when collision happens. In our simulation, α_i for all components were set to 1. And $f(Kn_{i,j},\alpha_i)$ is the transition regime correction factor to the Maxwellian flux as a function of the Knudsen Number:

$$f\left(Kn_{i,j},\alpha_i\right) = \frac{0.75\alpha_i(1+Kn_{i,j})}{Kn_{i,j}\left(1+Kn_{i,j}\right)+0.283\alpha_i Kn_{i,j}+0.75\alpha_i}, \quad (4)$$

$$Kn_{i,j} = \frac{\lambda_i}{\overline{R_{\mathrm{p},j}}}, \quad (5)$$

where λ_i is the mean free path.

Gas–wall partitioning follows an analogous framework:

$$\frac{\mathrm{d}C_{i,\mathrm{g}}}{\mathrm{d}t} = -k_{\mathrm{w}}\left(C_{i,\mathrm{g}} - \frac{C_{i,\mathrm{w}}}{C_{\mathrm{w}}}p_i^0\gamma_i\right), \quad (6)$$

$$\frac{\mathrm{d}C_{i,\mathrm{w}}}{\mathrm{d}t} = k_{\mathrm{w}}\left(C_{i,\mathrm{g}} - \frac{C_{i,\mathrm{w}}}{C_{\mathrm{w}}}p_i^0\gamma_i\right), \quad (7)$$

where p_i^0 is the liquid (sub-cooled if necessary) saturation vapour pressure of component i and γ_i is its activity coefficient on the wall. k_{w} ($\mathrm{s^{-1}}$) accounts for gas- and wall-phase diffusion, turbulence, accommodation coefficient, and chamber surface-area-to-volume ratio. k_{w} was set to $2.2\times10^{-3}\,\mathrm{s^{-1}}$ according to experimental measurement (Guo et al., 2022). Meanwhile, C_{w} ($\mathrm{g\,m^{-3}}$) represents wall adsorption/absorption properties, including effects of RH, surface area, diffusivity, and porosity. Neglecting the gas-wall partitioning of organic compounds in Teflon film chambers in the model can lead to a systematic overestimation of the yields of gaseous products and SOA (Matsunaga and Ziemann, 2010; Zhang et al., 2014). Therefore, we conducted a sensitivity analysis of SOA mass concentration by testing several different orders of magnitude for the C_{w} value (Fig. S2). When $C_{\mathrm{w}} = 0$, the simulated SOA mass concentration was still underestimated, which indicated that the source of SOA mass was underestimated in current model setup. The result for $C_{\mathrm{w}} = 1\times10^{-10}\,\mathrm{g\,m^{-3}}$ was nearly identical to that for $C_{\mathrm{w}} = 0$. However, to reflect the physical relevance of wall absorption in chamber studies, we used $C_{\mathrm{w}} = 1\times10^{-6}\,\mathrm{g\,m^{-3}}$ in our simulations, and the simulated SOA mass was reasonably reproduced. Increasing C_{w} by one order of magnitude to $1\times10^{-5}\,\mathrm{g\,m^{-3}}$ resulted in a larger deviation in SOA mass concentration, whereas decreasing it by one order of magnitude to $1\times10^{-7}\,\mathrm{g\,m^{-3}}$ led to only minimal changes in SOA mass concentration. Consequently, $C_{\mathrm{w}} = 1\times10^{-6}\,\mathrm{g\,m^{-3}}$ was finally selected for this study.

PyCHAM also simulates microphysical processes, including coagulation, nucleation, and particle wall loss, which influence particle number evolution. Using a semi-implicit equation, coagulation process accounts for Brownian diffusion, convective Brownian diffusion enhancement, gravitational collection, turbulent inertial motion, turbulent shear, and Vander Waals collisions (Jacobson, 2005), without adjustable parameters.

Nucleation is modeled using a tuned Gompertz function to fit measured particle number concentrations during the initial reaction phase, without inferring mechanistic details:

$$P_1(t) = \mathrm{nuc}_{v1}\left(\exp\left(\mathrm{nuc}_{v2}\left(\exp\left(-\frac{t}{\mathrm{nuc}_{v3}}\right)\right)\right)\right), \quad (8)$$

where P_1 ($\mathrm{no.\,cm^{-3}}$) is the number concentration of new particles after time t that enter the smallest size bin, and nuc_{vn} represents the user-defined parameters which allow the amplitude (nuc_{v1}), onset (nuc_{v2}) and duration (nuc_{v3})

of the curve to be adjusted. Note that Eq. (8) is independent of chemistry. In this study, particle number concentrations were firstly fitted to CPC measurements during the initial 0.57 h by setting nuc_{vn} ($\mathrm{nuc}_{v1} = 22\,403$, $\mathrm{nuc}_{v2} = -17.66$, $\mathrm{nuc}_{v3} = 317.88$). Particle size range of formed SOA was set as 1.8–500 nm, and the radius of newly nucleated particles was set as 10.9 nm according to lower limit of the size range of SMPS. PyCHAM employs a sectional approach, dividing particles into a number of size bins and simulating size evolution using the moving-center or full-moving approaches (Jacobson, 2005). As recommended by O'Meara et al. (2021) that a more detailed 128 size bins should be adopted when the number PSD is important, we set the bin number to 128 and employed the full-moving approach to simulate size evolution. In this way, the constrained and subsequently simulated number concentrations excluding coagulation agree well with CPC measurements ($R^2 = 0.89$; NMB = 0.29 %; Fig. S3). However, the PSD during the early nucleation stage cannot be set in nucleation scheme, and the PSD deviates significantly from measurements (Fig. S4).

Because the accuracy of CCN number concentration depends on both the SOA size distribution and κ, any bias in the PSD directly affects the CCN simulation. To improve the representation of early growth, nucleation scheme was not used and the initial number PSD was instead constrained using SMPS measurement during the initial 0.6 h assuming the species $C_{20}H_{30}O_{17}$ to represent low-volatile HOMs dimers as seed particle. The vapor pressure of $C_{20}H_{30}O_{17}$ at normal temperature calculated by default method of Nannoolal et al. (2008) is 2.14×10^{-29} Pa, which is extremely low to act as a seed aerosol. The lower and upper boundaries and mean radii of each size bin and bin number were set according to SMPS (9.82–429.4 nm size range and 106 size bins). Under this configuration, the PSD performed better than that of nucleation scheme (Fig. S5). However, the simulated SOA mass concentration and chemical composition were significantly influenced by the presence of assumed seed particles, increasing the discrepancy with measurements (Fig. S6). Therefore, to balance the simulation of chemical composition and PSD, the SOA mass concentration and chemical composition were simulated using the nucleation scheme (Sect. 3.1). In contrast, the particle number concentration and PSD were simulated using the SMPS-constrained approach (hereafter referred to as the seed scheme; Sect. 3.2). Subsequently, the κ values derived from the SOA chemical composition in Sect. 3.1 were combined with the PSD obtained in Sect. 3.2 to calculate CCN number concentrations (Sect. 3.3). The influence of individual schemes (nucleation or seed) on CCN predictions are in Sect. 3.4.

Particle wall deposition is simulated using either the McMurry and Rader (1985) model or a customized size-dependent deposition rate:

$$
\begin{aligned}
&D_\mathrm{p} < D_\mathrm{p,flec} \\
&\log_{10}\left(\beta\left(D_\mathrm{p}\right)\right) = \log_{10}\left(D_\mathrm{p,flec}\right) \\
&\qquad - \log_{10}\left(D_\mathrm{p}\right)\nabla_\mathrm{pre} + \beta_\mathrm{flec}, \qquad (9) \\
&D_\mathrm{p} \geq D_\mathrm{p,flec} \\
&\log_{10}\left(\beta\left(D_\mathrm{p}\right)\right) = \log_{10}\left(D_\mathrm{p}\right) \\
&\qquad - \log_{10}\left(D_\mathrm{p,flec}\right)\nabla_\mathrm{pro} + \beta_\mathrm{flec}, \qquad (10)
\end{aligned}
$$

where $D_{\mathrm{p},flec}$ marks the inflection diameter for deposition rates, and β_flec gives the deposition rate (s^{-1}) at this inflection point. ∇_pre and ∇_pro represent the log-log slopes of deposition rate versus diameter before and after the inflection point. As the PSD size range varied by only a factor of ~ 2 during the period when it was not constrained by SMPS measurements, and no obvious deviation in peak diameter was observed within ~ 1 h after the experiment ended, this study used a uniformed value ($\beta_\mathrm{flec} = 2.37 \times 10^{-5}\ \mathrm{s}^{-1}$) based on the measured particle loss rates without considering the size dependence.

Moreover, other parameters such as time series of temperature (291.2–299.1 K) and RH (37 %–79 %), and dilution rate ($9 \times 10^{-6}\ \mathrm{s}^{-1}$) during the experiment were constrained according to measurements.

The gas-phase chemical mechanism for α-pinene we used in PyCHAM draw upon previous studies as MCM coupled with PRAM mechanisms (Roldin et al., 2019; O'Meara et al., 2021; Luo et al., 2024; Thomsen et al., 2024). PyCHAM currently lacks explicit treatment of particle-phase reactions and dissolution, which are hence not considered in our simulation. The simulated α-pinene concentrations agree with measurements ($R^2 = 0.99$) in this study (Fig. S7), and the temporal trends of gas-phase products HOMs (Fig. S8) are well captured, though there are some biases in the absolute concentrations, indicating the capability to describe gas-phase chemistry of α-pinene ozonolysis by PyCHAM with MCM and PRAM mechanisms. The detailed chemical species formulas produced by MCM and PRAM mechanisms are shown in Table S1. And the input files including model variables setting and chemical mechanism files used in PyCHAM are supplied in the data availability section.

2.3 Hygroscopicity parameter (κ) and CCN concentration

The hygroscopicity parameter (κ) of bulk SOA was calculated using the UManSysProp module (Topping et al., 2016), an open-source tool for predicting molecular and atmospheric aerosol properties. UManSysProp estimates pure component vapor pressures, critical properties, sub-cooled densities of organic molecules; activity coefficients for mixed inorganic-organic liquid systems; hygroscopic growth factors and CCN activation potential of mixed inorganic–organic aerosol particles with associated κ–Köhler values

(Kreidenweis et al., 2005); and absorptive partitioning calculations with/without a treatment of non-ideality. Users input molecular information as SMILES (Simplified Molecular Input Line Entry System) strings, and UManSysProp automatically extracts relevant information for calculations.

In PyCHAM, UManSysProp predicts molecular weight, pure liquid density, and liquid saturation vapor pressure for individual components. Default methods include Girolami (1994) for liquid density and Nannoolal et al. (2008) for vapor pressure estimation. Since PyCHAM does not currently include κ prediction, we further calculated the κ values for bulk SOA under ideal condition given molar concentrations, vapor pressures, densities, temperatures, dry particle sizes, and a surface tension of 72 mN m^{-1}. The critical activated dry particle size ($D_{\mathrm{p},dry}$) for CCN activation at different SS levels was derived from the κ–Köhler equation (Petters and Kreidenweis, 2007):

$$\frac{\mathrm{RH}}{100} = \frac{D_{\mathrm{p,wet}}^3 - D_{\mathrm{p,dry}}^3}{D_{\mathrm{p,wet}}^3 - (1-\kappa)\, D_{\mathrm{p,dry}}^3} \exp\left(\frac{4\sigma_{\mathrm{s}} M_{\mathrm{w}}}{RT\rho_{\mathrm{w}} D_{\mathrm{p,wet}}}\right) \quad (11)$$

where σ_{s} is the surface tension of the wet particle at the solution-air interface, M_{w} is the molecular weight of water, R is the ideal gas constant, T is temperature, ρ_{w} is the density of water, and $D_{\mathrm{p,wet}}$ is the diameter of the wet particle.

Particles larger than $D_{\mathrm{p,dry}}$ can act as CCN and $D_{\mathrm{p,dry}}$ decreases with increasing SS. Then CCN number concentrations at different SS ($N_{\mathrm{CCN,SS}}$) were calculated by integrating the simulated particle number size distribution PNSD(D) over size bins exceeding $D_{\mathrm{p},dry}$:

$$N_{\mathrm{CCN,SS}} = \int_{D_{\mathrm{p,dry}}}^{D_{\max}} \mathrm{PNSD}(D)\mathrm{d}D \quad (12)$$

where D is dry particle diameter, and $D_{\max}$ is the maximum D.

3 Results and discussion

3.1 Simulation of particle formation and chemical composition

Figure 1 shows the simulated and measured SOA mass concentrations. The simulated SOA mass concentration exhibited a high correlation ($R^2 = 0.97$) with measurements and the two showed similar temporal trends, characterized by a rapid increase within the first ~ 3 h followed by a gradual decline. The simulated decline rate closely matched measurements (Fig. 1b), except for a faster decrease around ~ 6 h. This discrepancy is likely attributed to a rapid temperature increase during this period (Fig. S1), as elevated temperature can cause organic compounds to evaporate from the particle phase, reducing SOA formation (Donahue et al., 2006; Xia et al., 2008; Ceulemans et al., 2010). Simulated particle-phase HOMs accounted for ~ 43 % of total SOA mass concentration (Fig. 1a), highlighting the important contribution of HOMs to SOA and necessity of including HOM formation in the chemical mechanisms as done here by coupling MCM with the PRAM mechanism. Without PRAM mechanism, the onset of SOA growth was significantly delayed and mass concentration was obviously lower. The significant contribution of HOMs to SOA is consistent with previous studies. For example, Roldin et al. (2019) found ~ 50 % of SOA mass from α-pinene ozonolysis with ammonium sulfate seeds originates from HOM condensation. Gatzsche et al. (2017) reported HOMs contribute up to 65 % of SOA mass during early-stage α-pinene ozonolysis and account for about 27 % of the total SOA mass throughout the simulation.

Despite good correlation with measured SOA concentration, simulated SOA mass concentration was consistently underestimated (19.1 % ± 10.4 %). The underestimation can be attributed to incomplete description of gas-phase chemistry, gas-particle partitioning, and/or particle-phase chemistry. The gas-phase chemistry, including the loss of α-pinene (Fig. S7) and the composition of HOMs, is generally well reproduced (Fig. S9). The model reproduces the bimodal distributions of HOM monomers (m/z 230–380) and dimers (m/z 400–550), although the concentration of monomers is underestimated, especially below m/z 300. It also reasonably captures the fractions of HOM monomers and dimers (Fig. S10), while showing a slight overestimation of dimers in the simulation. This also indicates the capability of PRAM mechanism to effectively describe gas-phase HOM formation, as shown by Roldin et al. (2019).

The gas-particle partitioning in the model, which can be adjusted by activity coefficient (γ), also influences SOA mass concentration. The impact of non-ideal behavior on simulated gas-particle partitioning of SOA has been explored in previous studies (Zuend and Seinfeld, 2012; Lannuque et al., 2023). For example, Zuend and Seinfeld (2012) improved the accuracy of simulated mass and composition of SOA formed from α-pinene ozonolysis by accounting for non-ideal mixing and liquid–liquid phase separation through the calculation of γ for components in the liquid mixture using AIOMFAC (Aerosol Inorganic-Organic Mixtures Functional groups Activity Coefficients). Lannuque et al. (2023) also accounted for non-ideality (i.e., interactions between organic molecules and inorganic ions in the aqueous phase) in their simulation of SOA gas-particle partitioning. They found that considering only ideal partitioning leads to a substantial underestimation of SOA formation, particularly in the absence of a pre-existing organic phase. As no well-established data of γ were available for our experimental conditions, we only simulated the idealized conditions. Non-ideality was neglected, and γ for all species were set to 1. As shown in Eq. (2), lower γ (corresponding to higher solubility) would lead to higher SOA concentrations and thus reduce the gap between simulated and measured SOA mass concentrations. However, the simulated SOA mass concentration rise rate closely matched measurements (Fig. 1b), indicating the appropriate representation of gas-particle partitioning. There-

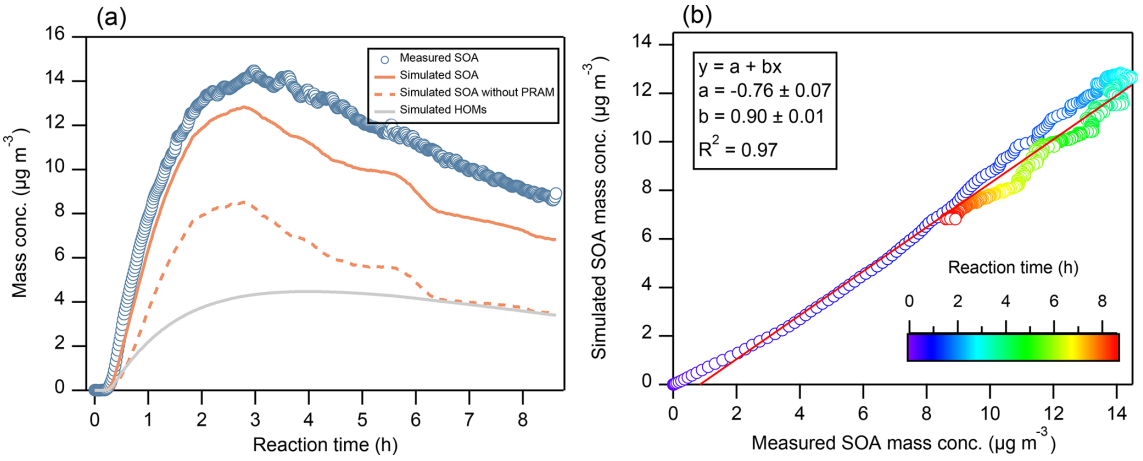

Figure 1. **(a)** Mass concentrations ($\mu g\,m^{-3}$) of simulated and measured SOA, together with the simulated particle-phase HOMs mass concentration. The dashed line refers to the simulated SOA excluding the PRAM mechanism. **(b)** Scatterplot of measured versus simulated SOA mass concentrations, with a linear regression fit (red line). The coefficients a and b denote the intercept and slope, respectively, and R^2 is the correlation coefficient. Colors indicate the reaction time during the experiment.

fore, the underestimation of SOA mass is possibly attributed to missing particle-phase chemistry.

Particle-phase accretion reactions or oligomerization processes can produce larger, higher-molecular-weight species, increasing SOA mass concentration (Pun and Seigneur, 2007; Kroll and Seinfeld, 2008; Hallquist et al., 2009). The influence of particle-phase reaction on SOA mass concentration has been reported in previous studies. For example, Hu et al. (2007) attributed up to 70 % of SOA mass to oligomers and polymers in toluene photooxidation, highlighting the importance of particle-phase reactions. By adjusting branching ratio for HOM formation and gas-wall partitioning parameters, Xu (2021) performed a good consistency between simulated and measured SOA mass concentrations from α-pinene ozonolysis. However, the simulated SOA mass concentration is still underestimated from their data even after considering OH-initiated secondary autoxidation, which might be due to the lack of particle-phase reactions in their simulation. Particle-phase reactions, including heterogeneous reactions on aerosol surfaces and in particles of organic compounds, can also alter SOA properties, such as solubility, viscosity, hygroscopicity, and optical properties (Farmer et al., 2015; Shrivastava et al., 2017; Jia and Xu, 2021). For example, Galeazzo et al. (2021) found that missing autoxidation and particle-phase reactions in α-pinene ozonolysis simulations leads to underestimated SOA viscosity.

Simulated O : C and H : C ratios of SOA were compared with measurements as AMS can only provide bulk O : C and H : C ratios of SOA rather than molecular chemical composition (Fig. 2). Compared to measured O : C (0.44 ± 0.03) and H : C (1.35 ± 0.02) ratios, the simulated average O : C (0.58 ± 0.03) and H : C (1.64 ± 0.00) ratios were overestimated. Without PRAM mechanism, the simulation showed lower O : C and higher H : C as a result of lacking gas-phase HOM formation, while still overestimating the two ratios. Figure S11 illustrates that the simulated O : C of gas-phase HOMs in the first 10 min of reaction is consistent with measurements, while the H : C is moderately overestimated. These results imply that inaccuracies in the simulated gas-phase chemistry may contribute to the overestimation ($21.2\,\% \pm 2.1\,\%$) of the H : C in SOA, but exert only a minor influence on the O : C in SOA. The overestimation ($32.4\,\% \pm 2.2\,\%$) of O : C is possibly attributed to the absence of particle-phase reactions in our simulations as mentioned above, emphasizing the importance of particle-phase chemistry in determining SOA chemical composition. The difference between modelled and measured O : C and H : C has also been reported by previous studies. Using similar gas-phase chemical mechanism, Roldin et al. (2019) reported similar overestimations in modelled H : C ratios, while modelled O : C ratios agree with measurements at the average level in their studies. Chen et al. (2011) observed overestimated O : C and H : C ratios in α-pinene ozonolysis simulations. However, HOMs are not included in the mechanism of their study. They proposed a chemical mechanism involving particle-phase decomposition of organic hydroperoxides and subsequent oligomerization involving free radicals to explain the discrepancies. Although HOMs formation was included in our study, the lack of similar particle-phase reactions can still contribute the discrepancies of H : C and O : C ratios.

Regarding the temporal changes, both the measured and simulated average O : C increased gradually over time before stabilizing, which is possibly attributed to the dilution of SOA concentration and/or the increasing fraction of particle-phase HOMs during the experiment (Fig. S12). In contrast, the measured H : C decreased over time, while the simulated H : C showed no apparent variations. Oxidation of particle-phase organics by atmospheric oxidants typically leads to

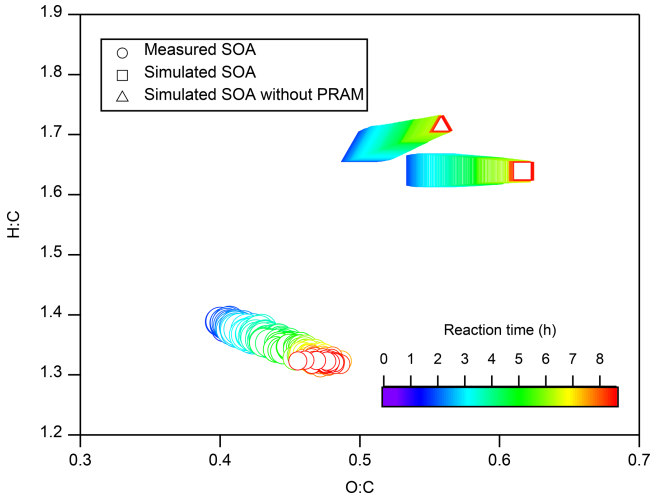

Figure 2. Chemical composition expressed as average O : C and H : C ratios for simulated (squares) and measured (circles) SOA, along with simulated SOA excluding the PRAM mechanism (triangles). Symbol sizes indicate SOA mass concentrations. Valid SOA measurements were available only after 0.45 h due to low SOA concentrations prior to that time.

an increase in O : C of organic matter by functionalization introducing oxygen-containing functional groups like -OH, -COOH, -ONO_2, -OOH, or leads to a decrease in O : C by fragmentation i.e. C-C bond breaking or peroxide photolysis (Kroll and Seinfeld, 2008; Hallquist et al., 2009), and their absence in simulations possibly contributes to the discrepancy between modelled and measured time series of O : C and corresponding H : C ratios.

3.2 Simulation of particle number concentrations and size distribution

Despite a slight underestimation (7.3 % ± 2.8 %) of the simulated number concentration as the model run freely following the constrained particle number size distribution, the simulated particle number concentration showed good agreement with measurements (Fig. 3), with a linear fit yielding a slope of 1.04 and a correlation coefficient of $R^2 = 0.99$. Our result is similar to the report of Xu (2021) which also exhibits an underestimation of particle number concentration when coagulation is included.

Particle number concentration is primarily influenced by microphysical processes such as nucleation, coagulation, and particle wall loss. In our simulation for particle number, the initial phase of particle growth was constrained by PSD of SMPS measurement instead of setting nucleation parameters, as detailed in Sect. 2.2. Besides, particle loss rate to wall was fully constrained by measurements. To explore the impact of coagulation on particle number concentration, we tested excluding coagulation in our simulation (Fig. S13). Coagulation, particularly among nanoparticles, increases collision probabilities, leading to the formation of larger particles and reduction in particle number concentration, and a shift in size distribution toward larger diameters (Jacobson, 2005; Seinfeld and Pandis, 2016). In this study, the simulated number concentration without coagulation declined more slowly than measurements throughout the whole simulation period (Fig. S13), resulting in an overestimation of 14.4 % ± 7.9 %, which is much more deviated from measured than that when including coagulation. In spite of using a semi-implicit coagulation equation (Jacobson, 2005) without adjustable parameters, our result suggests that the rates of coagulation of particles are well represented in PyCHAM model.

To further evaluate simulation accuracy of particle size, the geometric mean diameter of simulated SOA was calculated (Fig. 4), which showed good agreement with measurements ($R^2 = 0.96$) and a slight underestimation of 1.9 % ± 2.8 %, indicating an excellent reproduction of the central position of size distribution. Without PRAM mechanism, the geometric mean diameter of SOA was lower due to the absent production of larger molecules. When coagulation was excluded, the geometric mean diameter was underestimated by 8.8 % ± 1.1 % (Fig. S14), and was merely underestimated by 6.9 % ± 2.9 % compared to the result including coagulation, suggesting that particle growth during the reaction was primarily driven by condensation, overweighing the influence of coagulation on the size distribution. As a result, the size distribution showed only minor changes due to coagulation, which is in contrast with the large changes in particle number concentrations (Fig. S13).

Figure 5 compares the measured and simulated number size distributions of SOA, with shaded areas representing simulations and contour lines denoting measurements. The simulation effectively captured the trend of particle growth, and the simulated size range generally aligned with measurements. However, simulated PSD showed flatter and broader distribution patterns than measurement, even though it was constrained by SMPS during the initial 0.6 h. Figure S15 presents the $dN/d\log_{10}D_p$ versus PSD at 2, 4, 6, and 8 h of reaction time, clearly illustrating that the simulated PSDs were broader and flatter than measurement. When nucleation parameters were assigned to simulate initial particle growth in PyCHAM, instead of constraining the initial PSD with SMPS measurement, the simulated size distribution exhibited greater deviation from measured data (Figs. S4–S5). Xu (2021) assigned the nucleation parameters for the initial particle growth in PyCHAM, and found smaller particle size and a slower particle growth than measurement. These results indicate that no matter whether nucleation or seed particles are used to specify the initial number PSD in PyCHAM, the model currently still need improve representation of the evolution of particle size. Nevertheless, as the model has generally well reproduced the particle size and number concentration, it can be used for subsequent CCN simulations. When coagulation was excluded in our study, the simulated PSD showed some odd spikes in the early stage and more de-

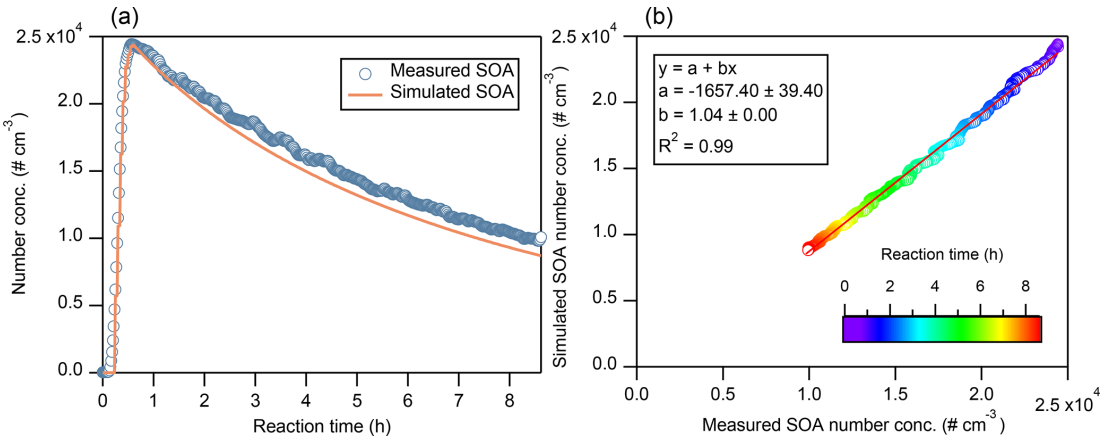

Figure 3. **(a–b)** Same as Fig. 1, but for SOA number concentration ($\#\,cm^{-3}$). Data points from the initial 0.6 h are excluded from the scatterplot because the number concentration during this period was fitted to the SMPS measurements and therefore assumed to match the measurements exactly. Note that coagulation is included in the simulation.

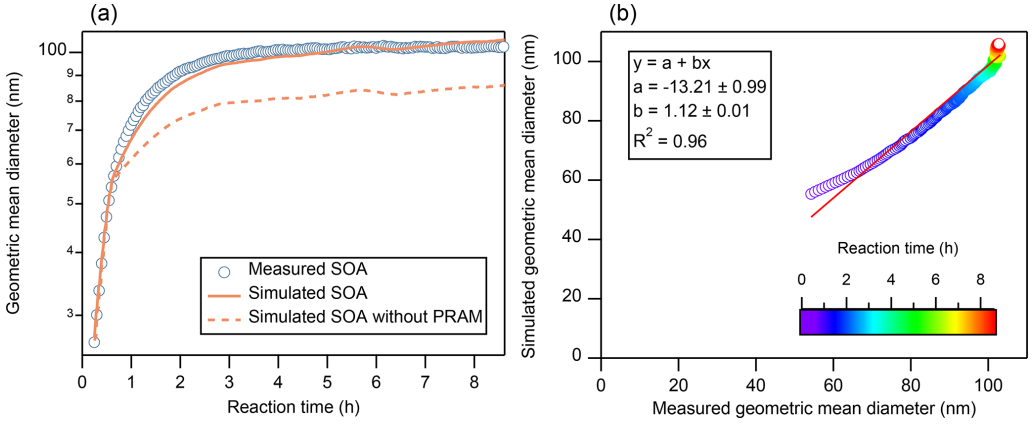

Figure 4. **(a–b)** Same as Fig. 1, but for the geometric mean diameter (nm) of SOA. The dashed line refers to the simulated SOA without the PRAM mechanism. Coagulation is included in the simulation. Data points from the initial 0.6 h are excluded from the scatterplot because the PSD during this period was fitted to the SMPS measurements.

viation from the measurement especially in the subsequent growth stage (Fig. S16), demonstrating the reliable representation of coagulation in PyCHAM model.

3.3 Simulation of κ and CCN concentrations

We calculated the hygroscopicity parameter (κ) of bulk SOA under ideal condition using the UManSysProp and compared with measurement (Fig. 6). The measured κ generally increased with higher SS, which is possibly attributed to the size dependence of chemical composition, consistent with previous monoterpene oxidation studies (Zhao et al., 2015; Zhang et al., 2023). In contrast, simulated κ was independent of SS and did not show a significant size dependence. From 50.6 to 84.8 nm of particle size, the κ derived from the chemical composition corresponding to size only decreased by 0.002, indicating weak dependence of simulated chemical composition on particle size, which is different from the measurement (Table S2). The sudden decrease in κ measured at $\sim$2 h of reaction is attributed to

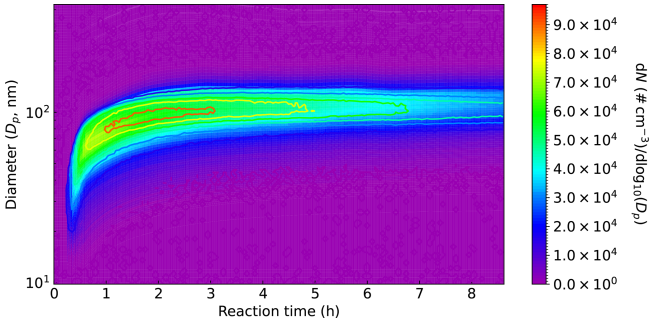

Figure 5. Time evolution of the number size distributions ($dN/d\log_{10}D_p$) for measured (contour lines) and simulated (shaded areas) SOA. Coagulation is included in the simulation.

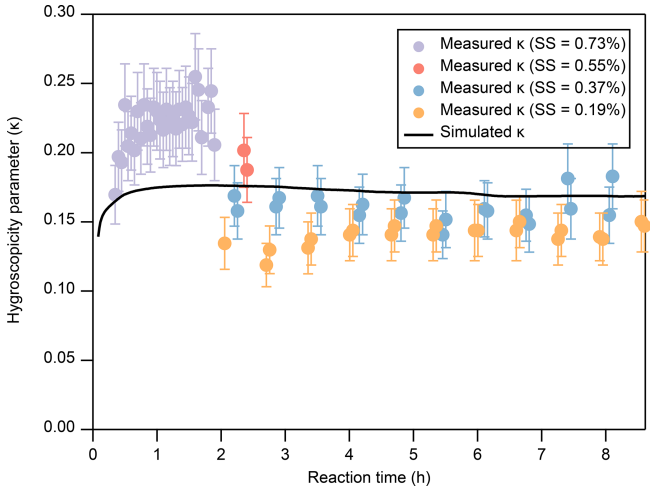

Figure 6. Hygroscopicity parameter (κ) of simulated SOA (line) and measured SOA (solid circles with standard-deviation error bars) at different supersaturation (SS). After ~ 2 h, κ values were showed only for SS $= 0.19$ % and 0.37 %, because the D_{crit} derived from fitting CCN / CN activation fraction curves at SS $= 0.73$ % and 0.55 % had too large uncertainties as almost all particles were activated.

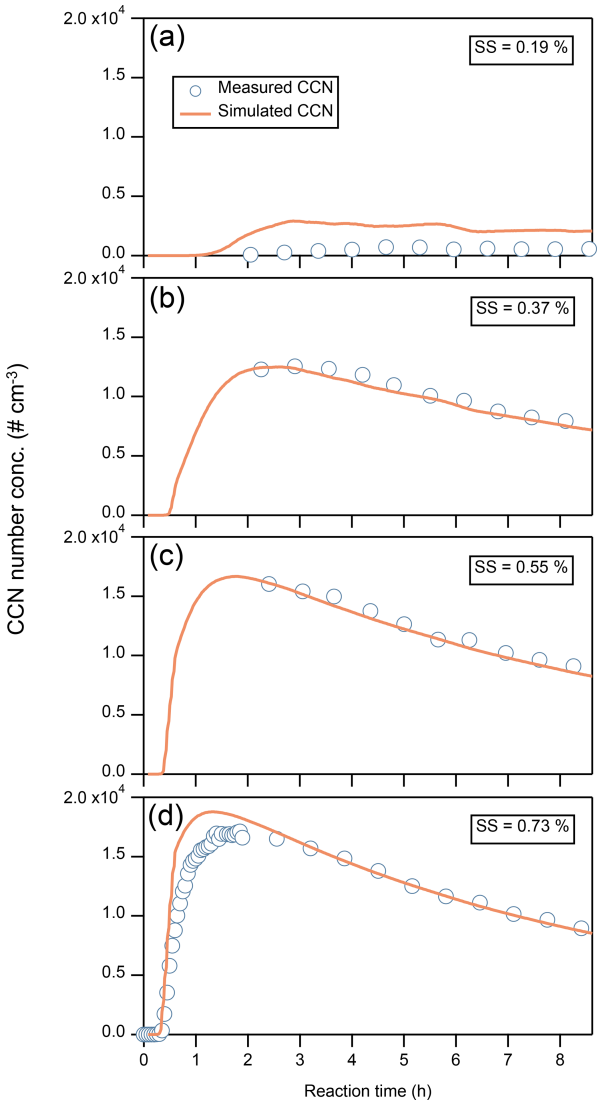

Figure 7. (a–d) Measured (circles) and simulated (lines) CCN number concentrations (# cm^{-3}) at different SS.

the decrease of the set SS from 0.73 % to 0.19 %. In contrast, the simulated κ was formula-based and did not correspond to specific SS. The simulated κ increased during the first hour before stabilizing at 0.172 ± 0.003. Compared to measurements, the simulated κ was underestimated by $20.7\,\% \pm 4.9\,\%$ at higher SS levels (0.73 % and 0.55 %), overestimated by $18.6\,\% \pm 5.9\,\%$ at SS $= 0.19$ %, and showed the closest agreement at SS $= 0.37$ %, with an overestimation of $9.6\,\% \pm 8.5\,\%$. Overall, the simulated κ agreed well with measurements, particularly at moderate SS (0.37 %).

Field observation and laboratory studies have shown that κ of SOA decreases with increasing molecular weight under supersaturated conditions (Kuwata et al., 2013; Wang et al., 2019). We computed the average molecular weight of SOA (Fig. S17) and found that the molecular weight decreased rapidly during the initial phase before stabilizing, explaining the measured and simulated increase in κ in the early stage in the experiment and its subsequent leveling off.

CCN number concentrations at different SS levels were derived using κ from the nucleation scheme and PSD from the seed scheme (Fig. 7). Figure S18 presents the PSD and D_{crit} at four SS levels corresponding to time points before and after 2 h, providing additional context for interpreting the discrepancies between simulated and measured CCN. At the higher SS levels of 0.73 % and 0.55 %, the simulated CCN number concentrations closely matched the measurements throughout the reaction ($R^2 = 0.88$–0.99), except for a more rapid increase during the initial period at SS $= 0.73$ %. Although κ was underestimated at these SS, leading to slightly overestimated D_{crit}, the simulated and measured D_{crit} were still very similar and both positioned to the left of the PSD peak (Fig. S18c and d). Under these conditions, the broader and flatter simulated PSD introduced a compensating effect, resulting in simulated CCN concentrations that were very close to the measurements. The slight overestimation of CCN before 0.6 h at SS $= 0.73$ % was primarily attributable to the low bias in simulated κ, since the simulated and measured PSD were identical during this period.

At SS $= 0.37$ %, the simulated CCN number concentrations also agreed closely with measured CCN ($R^2 = 0.98$) with a mean bias of $-3.9\,\% \pm 1.9\,\%$. This good agreement corresponds to the smallest discrepancy between simulated and measured κ at this SS. Although κ was slightly overestimated at SS $= 0.37$ %, the simulated and measured D_{crit} remained very similar and both lay to the left of the PSD peak

(Fig. S18b). As a result, the broader and flatter PSD did not introduce a noticeable bias in simulated CCN.

In contrast, at SS = 0.19 %, the simulated CCN number concentrations were obviously overestimated by a factor of > 4 throughout the reaction. At this lowest SS, the required D_{crit} is largest, and both simulated and measured D_{crit} were located to the right of the PSD peak (Fig. S18a). The high bias in simulated κ at this SS further reduced the simulated D_{crit}, and this underestimation, combined with the broader and flatter simulated PSD, resulted in pronounced overprediction of CCN relative to the measurements.

To further investigate the influence of κ values and PSD on CCN simulation results, we systematically examined different scenarios by either:

1. keeping κ fixed while varying the PSD using SMPS measurements or an 8-bin size distribution commonly used in chemical transport models (e.g., WRF-Chem), or

2. keeping the PSD fixed while applying different κ values, including κ derived from measurements or a fixed $\kappa = 0.1$, which is frequently used in chemical transport models.

For each scenario, CCN number concentrations were recalculated based on the modified κ or PSD. As shown in Fig. S19, when the PSD was varied while κ remained constant, the 106-bin particle size resolution employed in this study substantially outperformed the conventional 8-bin setting across all SS levels. The 106-bin results showed much closer agreement with CCN number concentrations derived from SMPS-measured PSDs, particularly during the early phase of CCN activation. At higher SS levels (0.73 % and 0.55 %), however, the influence of bin resolution became less significant, reflecting the reduced sensitivity of CCN activation to PSD when D_{crit} is sufficiently small such that most particles can act as CCN.

When κ was varied while the PSD was held constant (Fig. S20), CCN number concentrations calculated using κ from UManSysProp agreed very well with those derived from observationally inferred κ across all SS levels, except for an overestimation at the lowest SS. In contrast, the fixed $\kappa = 0.1$ approach consistently underestimated CCN number concentrations, with the discrepancies increasing at lower SS.

These findings indicate that accurate CCN simulation for SOA requires realistic representations of both κ and PSD, with their importance becoming particularly pronounced at low SS.

3.4 Discussion of the influence of individual schemes (nucleation vs. seed) on CCN predictions

To demonstrate the rationale for the combined approach – using κ from the nucleation scheme together with PSD from the seed scheme – a detailed analysis of the effect of applying each scheme independently on the CCN simulations is implemented.

As shown in Fig. S21, CCN calculated using the κ by the nucleation scheme (Fig. 6) and PSD by the same scheme (Fig. S4) at SS = 0.55 % and 0.73 % were comparable to those from the combined-scheme approach. However, at SS = 0.37 %, CCN was moderately overestimated, and at SS = 0.19 % the predicted CCN was initially higher than the measurements and then decreased toward zero. In contrast, CCN calculated using the κ from the seed scheme (Fig. S22) combined with its PSD (Fig. 5) produced lower CCN across all four SS (Fig. S23), leading to a worse performance than that of the combined-scheme approach.

Overall, if the nucleation scheme was applied alone, the simulated PSD performed worse than that obtained with the combined approach, resulting in deviations of CCN concentrations at the two lower SS. In contrast, applying the seed scheme alone led to worse simulations of initial SOA mass concentration, chemical composition, and κ due to the assumed composition of seed species. However, because the PSD remained relatively accurate, the resulting CCN concentrations were similar to those from the combined approach.

4 Conclusions and implications

In this study, we simulated mass concentration, number concentration, chemical composition (O : C and H : C ratios) and size distribution of SOA from α-pinene ozonolysis by coupling MCM and PRAM near-explicit chemical mechanisms in a process-level box model PyCHAM. We further simulated CCN number concentrations at a series of SS using hygroscopicity parameter (κ) of SOA calculated by UManSysProp according to κ-Köhler theory together with PSD. Compared to chamber experimental measurements, the SOA mass concentration was well reproduced with an underestimation of 19.1 % ± 10.4 %. O : C and H : C ratios were overestimated by 32.4 % ± 2.2 % and 21.2 % ± 2.1 %, respectively, and their time evolution was inconsistent with measurements. These discrepancies were possibly attributed to the absence of particle-phase reactions during the simulation, as gas-phase chemistry including α-pinene decay and HOMs composition were generally well reproduced. Moreover, simulated particle-phase HOMs contributed substantially (∼ 43 %) to SOA mass concentration, underscoring their critical role in SOA production.

With PSD and number concentration constrained by SMPS measurement during the initial reaction period, the simulated SOA number concentration exhibited good agreement with measurement ($R^2 = 0.99$). However, the simulated PSD showed broader and flatter patterns than measured one, suggesting the need for improving representation of size evolution in future PyCHAM development. Moreover, simulated κ showed overestimation (18.6 % ± 5.9 %) at the lowest

SS (0.19 %) and underestimation (20.7 % ± 4.9 %) at higher SS levels (0.73 % & 0.55 %), with the closest agreement at SS = 0.37 %. At SS = 0.19 %, CCN activation requires larger particle sizes; under this condition, both simulated and measured D_{crit} lie to the right of the PSD peak. The combination of an underestimated simulated D_{crit} and a broader and flatter simulated PSD leads to a substantial overestimation of CCN. In contrast, at the other SS levels, despite the broader and flatter simulated PSD, the simulated and measured D_{crit} are very similar and lie to the left of the PSD peak. Consequently, the broader and flatter simulated PSD partially compensate for the small differences in D_{crit}, resulting in CCN number concentrations that differ only slightly from the measurements ($R^2 = 0.88$–99).

To further quantify the individual contributions of κ and PSD on CCN, we conducted comparison analyses using different κ schemes and different numbers of particle size bins. We found that accurate representation of both κ and PSD is essential for reliable CCN simulations activated by SOA, particularly at low SS (< 0.4 %). At higher SS (> 0.4 %), the sensitivity of CCN predictions to these parameters decreased, because the reduced D_{crit} allows most particles to activate as CCN regardless of variations in κ or PSD.

This study advances previous research by simulating CCN formation from SOA using a near-explicit and process-level model for the first time to our knowledge, and demonstrates the potential of this approach to inform the development of parameterizations in chemical transport models. Although current model still has some limitations, such as the absence of particle-phase chemistry, lack of explicit treatment of activity coefficients, and the inability to prescribe physically based nucleation and initial PSD, the model reproduces key features of the measured SOA and CCN reasonably well. Our findings further indicate that simplified representations of PSD and κ are insufficient for accurately describing CCN. These results suggest that HOMs chemistry, finer PSD resolution and improved κ parameterizations in chemical transport models are warranted. Improvement in process-level model e.g. including particle-phase chemistry, explicit treatment of activity coefficients, and allowing prescribing physically based nucleation and initial PSD are warranted in future work to provide a benchmark model to evaluate various parameterizations related to SOA formation and CCN concentrations. And future work could also extend this analysis to a range of biogenic and anthropogenic VOCs oxidation systems to develop generalized PSD and κ parameterization modules, potentially through training AI-based methods capable of learning sophisticated and process-informed parameterizations, which may be used to improve chemical transport models.

Data availability. The input files including model variables setting and chemical mechanism files used in PyCHAM are available on Zenodo at https://doi.org/10.5281/zenodo.17539325 (Song et al., 2026). And all the data in the figures of this study are available upon request to the corresponding author (dfzhao@fudan.edu.cn).

Supplement. The supplement related to this article is available online at https://doi.org/10.5194/acp-26-2769-2026-supplement.

Author contributions. DZ conceptualized the study. ZS performed the model simulation. CZ analyzed the measured CCN data and calculated the hygroscopicity parameter. HM analyzed the mass spectra data of gas-phase HOMs. ZS wrote the manuscript. ZS and DZ edited the manuscript with the input from all co-authors. All the co-authors discussed the results and commented on the manuscript.

Competing interests. The contact author has declared that none of the authors has any competing interests.

Disclaimer. Publisher's note: Copernicus Publications remains neutral with regard to jurisdictional claims made in the text, published maps, institutional affiliations, or any other geographical representation in this paper. The authors bear the ultimate responsibility for providing appropriate place names. Views expressed in the text are those of the authors and do not necessarily reflect the views of the publisher.

Acknowledgements. We thank Thomas F. Mentel for the support of this study. We gratefully acknowledge Simon Patrick O'Meara for updating the code and function of PyCHAM and the support of the xml file in simulation. We gratefully thank Simon Patrick O'Meara and the anonymous reviewer for their constructive comments and valuable suggestions, which have significantly improved the quality of our manuscript.

Financial support. This research has been supported by the Science and Technology Commission of Shanghai Municipality (Shanghai Pilot Program for Basic Research-Fudan University, grant no. 21TQ1400100 (22TQ010)) and the National Natural Science Foundation of China (grant no. 42575109).

Review statement. This paper was edited by Hang Su and reviewed by Simon O'Meara and one anonymous referee.

References

Aumont, B., Szopa, S., and Madronich, S.: Modelling the evolution of organic carbon during its gas-phase tropospheric oxidation: development of an explicit model based on a self generating approach, Atmos. Chem. Phys., 5, 2497–2517, https://doi.org/10.5194/acp-5-2497-2005, 2005.

Bianchi, F., Kurtén, T., Riva, M., Mohr, C., Rissanen, M. P., Roldin, P., Berndt, T., Crounse, J. D., Wennberg, P. O., Mentel, T. F.,

Wildt, J., Junninen, H., Jokinen, T., Kulmala, M., Worsnop, D. R., Thornton, J. A., Donahue, N., Kjaergaard, H. G., and Ehn, M.: Highly oxygenated organic molecules (HOM) from gas-phase autoxidation involving peroxy radicals: a key contributor to atmospheric aerosol, Chem. Rev., 119, 3472–3509, https://doi.org/10.1021/acs.chemrev.8b00395, 2019.

Camredon, M., Aumont, B., Lee-Taylor, J., and Madronich, S.: The SOA/VOC/NO_x system: an explicit model of secondary organic aerosol formation, Atmos. Chem. Phys., 7, 5599–5610, https://doi.org/10.5194/acp-7-5599-2007, 2007.

Capouet, M., Peeters, J., Nozière, B., and Müller, J.-F.: Alpha-pinene oxidation by OH: simulations of laboratory experiments, Atmos. Chem. Phys., 4, 2285–2311, https://doi.org/10.5194/acp-4-2285-2004, 2004.

Capouet, M., Mueller, J. F., Ceulemans, K., Compernolle, S., Vereecken, L., and Peeters, J.: Modeling aerosol formation in alpha-pinene photo-oxidation experiments, J. Geophys. Res.-Atmos., 113, D02308, https://doi.org/10.1029/2007jd008995, 2008.

Ceulemans, K., Compernolle, S., Peeters, J., and Müller, J.-F.: Evaluation of a detailed model of secondary organic aerosol formation from α-pinene against dark ozonolysis experiments, Atmos. Environ., 44, 5434–5442, https://doi.org/10.1016/j.atmosenv.2010.05.001, 2010.

Chen, Q., Liu, Y. D., Donahue, N. M., Shilling, J. E., and Martin, S. T.: Particle-phase chemistry of secondary organic material: modeled compared to measured O : C and H : C elemental ratios provide constraints, Environ. Sci. Technol., 45, 4763–4770, https://doi.org/10.1021/es104398s, 2011.

DeCarlo, P. F., Kimmel, J. R., Trimborn, A., Northway, M. J., Jayne, J. T., Aiken, A. C., Gonin, M., Fuhrer, K., Horvath, T., Docherty, K. S., Worsnop, D. R., and Jimenez, J. L.: Field-deployable, high-resolution, time-of-flight aerosol mass spectrometer, Anal. Chem., 78, 8281–8289, https://doi.org/10.1021/ac061249n, 2006.

Donahue, N. M., Robinson, A. L., Stanier, C. O., and Pandis, S. N.: Coupling partitioning, dilution, and chemical aging of semivolatile organics, Environ. Sci. Technol., 40, 2635–2643, https://doi.org/10.1021/es052297c, 2006.

Ehn, M., Thornton, J. A., Kleist, E., Sipilä, M., Junninen, H., Pullinen, I., Springer, M., Rubach, F., Tillmann, R., Lee, B., Lopez-Hilfiker, F., Andres, S., Acir, I. H., Rissanen, M., Jokinen, T., Schobesberger, S., Kangasluoma, J., Kontkanen, J., Nieminen, T., Kurtén, T., Nielsen, L. B., Jørgensen, S., Kjaergaard, H. G., Canagaratna, M., Dal Maso, M., Berndt, T., Petäjä, T., Wahner, A., Kerminen, V. M., Kulmala, M., Worsnop, D. R., Wildt, J., and Mentel, T. F.: A large source of low-volatility secondary organic aerosol, Nature, 506, 476–485, https://doi.org/10.1038/nature13032, 2014.

Fanourgakis, G. S., Kanakidou, M., Nenes, A., Bauer, S. E., Bergman, T., Carslaw, K. S., Grini, A., Hamilton, D. S., Johnson, J. S., Karydis, V. A., Kirkevåg, A., Kodros, J. K., Lohmann, U., Luo, G., Makkonen, R., Matsui, H., Neubauer, D., Pierce, J. R., Schmale, J., Stier, P., Tsigaridis, K., van Noije, T., Wang, H., Watson-Parris, D., Westervelt, D. M., Yang, Y., Yoshioka, M., Daskalakis, N., Decesari, S., Gysel-Beer, M., Kalivitis, N., Liu, X., Mahowald, N. M., Myriokefalitakis, S., Schrödner, R., Sfakianaki, M., Tsimpidi, A. P., Wu, M., and Yu, F.: Evaluation of global simulations of aerosol particle and cloud condensation nuclei number, with implications for cloud droplet formation, Atmos. Chem. Phys., 19, 8591–8617, https://doi.org/10.5194/acp-19-8591-2019, 2019.

Farmer, D. K., Cappa, C. D., and Kreidenweis, S. M.: Atmospheric processes and their controlling influence on cloud condensation nuclei activity, Chem. Rev., 115, 4199–4217, https://doi.org/10.1021/cr5006292, 2015.

Fuchs, H., Dorn, H.-P., Bachner, M., Bohn, B., Brauers, T., Gomm, S., Hofzumahaus, A., Holland, F., Nehr, S., Rohrer, F., Tillmann, R., and Wahner, A.: Comparison of OH concentration measurements by DOAS and LIF during SAPHIR chamber experiments at high OH reactivity and low NO concentration, Atmos. Meas. Tech., 5, 1611–1626, https://doi.org/10.5194/amt-5-1611-2012, 2012.

Fuchs, N. A. and Sutugin, A. G.: High dispersed aerosols, in: Topics in Current Aerosol Research, edited by: Hidy, G. M. and Brock, J. R., Pergamon, New York, ISBN 1483146170, 1971.

Galeazzo, T., Valorso, R., Li, Y., Camredon, M., Aumont, B., and Shiraiwa, M.: Estimation of secondary organic aerosol viscosity from explicit modeling of gas-phase oxidation of isoprene and α-pinene, Atmos. Chem. Phys., 21, 10199–10213, https://doi.org/10.5194/acp-21-10199-2021, 2021.

Gatzsche, K., Iinuma, Y., Tilgner, A., Mutzel, A., Berndt, T., and Wolke, R.: Kinetic modeling studies of SOA formation from α-pinene ozonolysis, Atmos. Chem. Phys., 17, 13187–13211, https://doi.org/10.5194/acp-17-13187-2017, 2017.

Girolami, G. S.: A simple "back of the envelope" method for estimating the densities and molecular volumes of liquids and solids, J. Chem. Educ., 71, 962–964, https://doi.org/10.1021/ed071p962, 1994.

Griffin, R. J., Dabdub, D., and Seinfeld, J. H.: Secondary organic aerosol 1. Atmospheric chemical mechanism for production of molecular constituents, J. Geophys. Res., 107, 4332, https://doi.org/10.1029/2001JD000541, 2002.

Guo, Y., Shen, H., Pullinen, I., Luo, H., Kang, S., Vereecken, L., Fuchs, H., Hallquist, M., Acir, I.-H., Tillmann, R., Rohrer, F., Wildt, J., Kiendler-Scharr, A., Wahner, A., Zhao, D., and Mentel, T. F.: Identification of highly oxygenated organic molecules and their role in aerosol formation in the reaction of limonene with nitrate radical, Atmos. Chem. Phys., 22, 11323–11346, https://doi.org/10.5194/acp-22-11323-2022, 2022.

Hallquist, M., Wenger, J. C., Baltensperger, U., Rudich, Y., Simpson, D., Claeys, M., Dommen, J., Donahue, N. M., George, C., Goldstein, A. H., Hamilton, J. F., Herrmann, H., Hoffmann, T., Iinuma, Y., Jang, M., Jenkin, M. E., Jimenez, J. L., Kiendler-Scharr, A., Maenhaut, W., McFiggans, G., Mentel, Th. F., Monod, A., Prévôt, A. S. H., Seinfeld, J. H., Surratt, J. D., Szmigielski, R., and Wildt, J.: The formation, properties and impact of secondary organic aerosol: current and emerging issues, Atmos. Chem. Phys., 9, 5155–5236, https://doi.org/10.5194/acp-9-5155-2009, 2009.

Hodzic, A. and Jimenez, J. L.: Modeling anthropogenically controlled secondary organic aerosols in a megacity: a simplified framework for global and climate models, Geosci. Model Dev., 4, 901–917, https://doi.org/10.5194/gmd-4-901-2011, 2011.

Hu, D., Tolocka, M., Li, Q., and Kamens, R. M.: A kinetic mechanism for predicting secondary organic aerosol formation from toluene oxidation in the presence of NO_x

and natural sunlight, Atmos. Environ., 41, 6478–6496, https://doi.org/10.1016/j.atmosenv.2007.04.025, 2007.

Huang, R. J., Zhang, Y., Bozzetti, C., Ho, K. F., Cao, J. J., Han, Y., Daellenbach, K. R., Slowik, J. G., Platt, S. M., Canonaco, F., Zotter, P., Wolf, R., Pieber, S. M., Bruns, E. A., Crippa, M., Ciarelli, G., Piazzalunga, A., Schwikowski, M., Abbaszade, G., Schnelle-Kreis, J., Zimmermann, R., An, Z. S., Szidat, S., Baltensperger, U., ElHaddad, I., and Prévôt, A. S. H.: High secondary aerosol contribution to particulate pollution during haze events in China, Nature, 514, 218–222, https://doi.org/10.1038/nature13774, 2014.

IPCC: Climate change 2021: The physical science basis, Contribution of working group I to the sixth assessment report of the Intergovernmental Panel on Climate Change, Cambridge University Press, https://doi.org/10.1017/9781009157896, 2021.

Jacobson, M.: Fundamentals of atmospheric modeling, Cambridge University Press, https://doi.org/10.1017/CBO9781139165389, 2005.

Jenkin, M. E.: Modelling the formation and composition of secondary organic aerosol from α- and β-pinene ozonolysis using MCM v3, Atmos. Chem. Phys., 4, 1741–1757, https://doi.org/10.5194/acp-4-1741-2004, 2004.

Jenkin, M. E., Saunders, S. M., and Pilling, M. J.: The tropospheric degradation of volatile organic compounds: A protocol for mechanism development, Atmos. Environ., 31, 81–104, https://doi.org/10.1016/S1352-2310(96)00105-7, 1997.

Jenkin, M. E., Saunders, S. M., Wagner, V., and Pilling, M. J.: Protocol for the development of the Master Chemical Mechanism, MCM v3 (Part B): tropospheric degradation of aromatic volatile organic compounds, Atmos. Chem. Phys., 3, 181–193, https://doi.org/10.5194/acp-3-181-2003, 2003.

Jia, L. and Xu, Y. F.: A core-shell box model for simulating viscosity dependent secondary organic aerosol (CSVA) and its application, Sci. Total Environ., 789, 147954, https://doi.org/10.1016/j.scitotenv.2021.147954, 2021.

Jimenez, J. L., Canagaratna, M. R., Donahue, N. M., Prevot, A. S. H., Zhang, Q., Kroll, J. H., DeCarlo, P. F., Allan, J. D., Coe, H., Ng, N. L., Aiken, A. C., Docherty, K. S., Ulbrich, I. M., Grieshop, A. P., Robinson, A. L., Duplissy, J., Smith, J. D., Wilson, K. R., Lanz, V. A., Hueglin, C., Sun, Y. L., Tian, J., Laaksonen, A., Raatikainen, T., Rautiainen, J., Vaattovaara, P., Ehn, M., Kulmala, M., Tomlinson, J. M., Collins, D. R., Cubison, M. J., Dunlea, E. J., Huffman, J. A., Onasch, T. B., Alfarra, M. R., Williams, P. I., Bower, K., Kondo, Y., Schneider, J., Drewnick, F., Borrmann, S., Weimer, S., Demerjian, K., Salcedo, D., Cottrell, L., Griffin, R., Takami, A., Miyoshi, T., Hatakeyama, S., Shimono, A., Sun, J. Y., Zhang, Y. M., Dzepina, K., Kimmel, J. R., Sueper, D., Jayne, J. T., Herndon, S. C., Trimborn, A. M., Williams, L. R., Wood, E. C., Middlebrook, A. M., Kolb, C. E., Baltensperger, U., and Worsnop, D. R.: Evolution of organic aerosols in the atmosphere, Science, 326, 1525–1529, https://doi.org/10.1126/science.1180353, 2009.

Johnson, D., Jenkin, M. E., Wirtz, K., and Martin-Reviejo, M.: Simulating the formation of secondary organic aerosol from the photooxidation of toluene, Environmental Chemistry, 1, 150–165, https://doi.org/10.1071/EN04069, 2004.

Johnson, D., Jenkin, M. E., Wirtz, K., and Martín-Reviejo, M.: Simulating the formation of secondary organic aerosol from the photooxidation of aromatic hydrocarbons, Environmental Chemistry, 2, 35–48, https://doi.org/10.1071/EN04079, 2005.

Kanakidou, M., Seinfeld, J. H., Pandis, S. N., Barnes, I., Dentener, F. J., Facchini, M. C., Van Dingenen, R., Ervens, B., Nenes, A., Nielsen, C. J., Swietlicki, E., Putaud, J. P., Balkanski, Y., Fuzzi, S., Horth, J., Moortgat, G. K., Winterhalter, R., Myhre, C. E. L., Tsigaridis, K., Vignati, E., Stephanou, E. G., and Wilson, J.: Organic aerosol and global climate modelling: a review, Atmos. Chem. Phys., 5, 1053–1123, https://doi.org/10.5194/acp-5-1053-2005, 2005.

Kelly, J. L., Michelangeli, D. V., Makar, P. A., Hastie, D. R., Mozurkewich, M., and Auld, J.: Aerosol speciation and mass prediction from toluene oxidation under high NO_x conditions, Atmos. Environ., 44, 361–369, https://doi.org/10.1016/j.atmosenv.2009.10.035, 2010.

Kreidenweis, S. M., Koehler, K., DeMott, P. J., Prenni, A. J., Carrico, C., and Ervens, B.: Water activity and activation diameters from hygroscopicity data – Part I: Theory and application to inorganic salts, Atmos. Chem. Phys., 5, 1357–1370, https://doi.org/10.5194/acp-5-1357-2005, 2005.

Kroll, J. H. and Seinfeld, J. H.: Chemistry of secondary organic aerosol: Formation and evolution of low-volatility organics in the atmosphere, Atmos. Environ., 42, 3593–3624, https://doi.org/10.1016/j.atmosenv.2008.01.003, 2008.

Kuang, Y., Xu, W., Tao, J., Ma, N., Zhao, C., and Shao, M.: A review on laboratory studies and field measurements of atmospheric organic aerosol hygroscopicity and its parameterization based on oxidation levels, Curr. Pollution Rep. 6, 410–424, https://doi.org/10.1007/s40726-020-00164-2, 2020.

Kuwata, M., Shao, W., Lebouteiller, R., and Martin, S. T.: Classifying organic materials by oxygen-to-carbon elemental ratio to predict the activation regime of Cloud Condensation Nuclei (CCN), Atmos. Chem. Phys., 13, 5309–5324, https://doi.org/10.5194/acp-13-5309-2013, 2013.

La, Y. S., Camredon, M., Ziemann, P. J., Valorso, R., Matsunaga, A., Lannuque, V., Lee-Taylor, J., Hodzic, A., Madronich, S., and Aumont, B.: Impact of chamber wall loss of gaseous organic compounds on secondary organic aerosol formation: explicit modeling of SOA formation from alkane and alkene oxidation, Atmos. Chem. Phys., 16, 1417–1431, https://doi.org/10.5194/acp-16-1417-2016, 2016.

Lannuque, V., D'Anna, B., Kostenidou, E., Couvidat, F., Martinez-Valiente, A., Eichler, P., Wisthaler, A., Müller, M., Temime-Roussel, B., Valorso, R., and Sartelet, K.: Gas–particle partitioning of toluene oxidation products: an experimental and modeling study, Atmos. Chem. Phys., 23, 15537–15560, https://doi.org/10.5194/acp-23-15537-2023, 2023.

Liu, X. H. and Wang, J.: How important is organic aerosol hygroscopicity to aerosol indirect forcing?, Environ. Res. Lett., 5, 044010, https://doi.org/10.1088/1748-9326/5/4/044010, 2010.

Lopez, B., Bhattacharyya, N., DeVivo, J., Wang, M., Caudillo-Plath, L., Surdu, M., Bianchi, F., Brasseur, Z., Buchholz, A., Chen, D., Duplissy, J., He, X.-C., Hofbauer, V., Mahfouz, N., Makhmutov, V., Marten, R., Mentler, B., Philippov, M., Schervish, M., Wang, D. S., Weber, S. K., Welti, A., El Haddad, I., Lehtipalo, K., Kulmala, M., Worsnop, D., Kirkby, J., Mauldin, R. L., Stolzenburg, D., Schobesberger, S., Flagan, R., and Donahue, N. M.: A diagonal volatility basis set to assess the conden-

sation of organic vapors onto particles, Environ. Sci.: Atmos., 5, 1035-1061, https://doi.org/10.1039/D5EA00062A, 2025.

Lowe, D., Topping, D., and McFiggans, G.: Modelling multi-phase halogen chemistry in the remote marine boundary layer: investigation of the influence of aerosol size resolution on predicted gas- and condensed-phase chemistry, Atmos. Chem. Phys., 9, 4559–4573, https://doi.org/10.5194/acp-9-4559-2009, 2009.

Luo, G. and Yu, F.: Simulation of particle formation and number concentration over the Eastern United States with the WRF-Chem + APM model, Atmos. Chem. Phys., 11, 11521–11533, https://doi.org/10.5194/acp-11-11521-2011, 2011.

Luo, Y., Thomsen, D., Iversen, E. M., Roldin, P., Skønager, J. T., Li, L., Priestley, M., Pedersen, H. B., Hallquist, M., Bilde, M., Glasius, M., and Ehn, M.: Formation and temperature dependence of highly oxygenated organic molecules (HOMs) from Δ^3-carene ozonolysis, Atmos. Chem. Phys., 24, 9459–9473, https://doi.org/10.5194/acp-24-9459-2024, 2024.

Matsunaga, A. and Ziemann, P. J.: Gas-wall partitioning of organic compounds in a teflon film chamber and potential effects on reaction product and aerosol yield measurements, Aerosol Science and Technology, 44, 881–892, https://doi.org/10.1080/02786826.2010.501044, 2010.

McFiggans, G., Artaxo, P., Baltensperger, U., Coe, H., Facchini, M. C., Feingold, G., Fuzzi, S., Gysel, M., Laaksonen, A., Lohmann, U., Mentel, T. F., Murphy, D. M., O'Dowd, C. D., Snider, J. R., and Weingartner, E.: The effect of physical and chemical aerosol properties on warm cloud droplet activation, Atmos. Chem. Phys., 6, 2593–2649, https://doi.org/10.5194/acp-6-2593-2006, 2006.

McMurry, P. and Rader, D.: Aerosol wall losses in electrically charged chambers, Aerosol Sci. Tech., 4, 249–268, https://doi.org/10.1080/02786828508959054, 1985.

Mei, F., Setyan, A., Zhang, Q., and Wang, J.: CCN activity of organic aerosols observed downwind of urban emissions during CARES, Atmos. Chem. Phys., 13, 12155–12169, https://doi.org/10.5194/acp-13-12155-2013, 2013.

Moore, R., Nenes, A., and Medina, J.: Scanning Mobility CCN Analysis – A method for fast measurements of size resolved CCN distributions and activation kinetics, Aerosol Sci. Tech., 44, 861–871, https://doi.org/10.1080/02786826.2010.498715, 2010.

Nannoolal, Y., Rarey, J., and Ramjugernath, D.: Estimation of pure component properties: Part 3. Estimation of the vapour pressure of non-electrolyte organic compounds via group contributions and group interactions, Fluid Phase Equilibr., 269, 117–133, https://doi.org/10.1016/j.fluid.2008.04.020, 2008.

O'Meara, S. P., Xu, S., Topping, D., Alfarra, M. R., Capes, G., Lowe, D., Shao, Y., and McFiggans, G.: PyCHAM (v2.1.1): a Python box model for simulating aerosol chambers, Geosci. Model Dev., 14, 675–702, https://doi.org/10.5194/gmd-14-675-2021, 2021.

Pankow, J. F.: An absorption model of gas/particle partitioning involved in the formation of secondary organic aerosol, Atmos. Env., 28, 189–193, https://doi.org/10.1016/j.atmosenv.2007.10.060, 1994.

Peeters, J., Vereecken, L., and Fantechi, G.: The detailed mechanism of the OH-initiated atmospheric oxidation of α-pinene: A theoretical study, Phys. Chem. Chem. Phys., 3, 5489–5504, https://doi.org/10.1039/B106555F, 2001.

Petters, M. D. and Kreidenweis, S. M.: A single parameter representation of hygroscopic growth and cloud condensation nucleus activity, Atmos. Chem. Phys., 7, 1961–1971, https://doi.org/10.5194/acp-7-1961-2007, 2007.

Pichelstorfer, L., Roldin, P., Rissanen, M., Hyttinen, N., Garmash, O., Xavier, C., Zhou, P., Clusius, P., Foreback, B., Golin Almeida, T., Deng, C., Baykara, M., Kurten, T., and Boy, M.: Towards automated inclusion of autoxidation chemistry in models: from precursors to atmospheric implications, Environ. Sci.: Atmos., 4, 879–896, https://doi.org/10.1039/D4EA00054D, 2024.

Pun, B. K. and Seigneur, C.: Investigative modeling of new pathways for secondary organic aerosol formation, Atmos. Chem. Phys., 7, 2199–2216, https://doi.org/10.5194/acp-7-2199-2007, 2007.

Rohrer, F., Bohn, B., Brauers, T., Brüning, D., Johnen, F.-J., Wahner, A., and Kleffmann, J.: Characterisation of the photolytic HONO-source in the atmosphere simulation chamber SAPHIR, Atmos. Chem. Phys., 5, 2189–2201, https://doi.org/10.5194/acp-5-2189-2005, 2005.

Roldin, P., Ehn, M., Kurten, T., Olenius, T., Rissanen, M. P., Sarnela, N., Elm, J., Rantala, P., Hao, L., Hyttinen, N., Heikkinen, L., Worsnop, D. R., Pichelstorfer, L., Xavier, C., Clusius, P., Ostrom, E., Petaja, T., Kulmala, M., Vehkamaki, H., Virtanen, A., Riipinen, I., and Boy, M.: The role of highly oxygenated organic molecules in the Boreal aerosol-cloud-climate system, Nat. Commun., 10, 4370, https://doi.org/10.1038/s41467-019-12338-8, 2019.

Saunders, S. M., Jenkin, M. E., Derwent, R. G., and Pilling, M. J.: Protocol for the development of the Master Chemical Mechanism, MCM v3 (Part A): tropospheric degradation of non-aromatic volatile organic compounds, Atmos. Chem. Phys., 3, 161–180, https://doi.org/10.5194/acp-3-161-2003, 2003.

Seinfeld, J. H. and Pandis, S. N.: Atmospheric chemistry and physics: From air pollution to climate change, 3rd edn., Wiley, ISBN 978-1-118-94740-1, 2016.

Shrivastava, M., Cappa, C. D., Fan, J., Goldstein, A. H., Guenther, A. B., Jimenez, J. L., Kuang, C., Laskin, A., Martin, S. T., Ng, N. L., Petaja, T., Pierce, J. R., Rasch, P. J., Roldin, P., Seinfeld, J. H., Shilling, J., Smith, J. N., Thornton, J. A., Volkamer, R., Wang, J., Worsnop, D. R., Zaveri, R. A., Zelenyuk, A., and Zhang, Q.: Recent advances in understanding secondary organic aerosol: Implications for global climate forcing, Rev. Geophys., 55, 509–559, https://doi.org/10.1002/2016RG000540, 2017.

Song, Z., Zhang, C., Shen, H., Ma, H., Pullinen, I., and Zhao, D.: Process-level simulation of chemical composition, size distribution and cloud condensation nuclei of secondary organic aerosol from α-pinene ozonolysis, Zenodo [data set], https://doi.org/10.5281/zenodo.17539325, 2026.

Thomsen, D., Iversen, E. M., Skønager, J. T., Luo, Y., Li, L., Roldin, P., Priestley, M., Pedersen, H. B., Hallquist, M., and Ehn, M.: The effect of temperature and relative humidity on secondary organic aerosol formation from ozonolysis of Δ^3-carene, Environmental Science: Atmospheres, 4, 88–103, https://doi.org/10.1039/D3EA00128H, 2024.

Topping, D. and Bane, M.: Introduction to aerosol modelling: From theory to code, Wiley, https://doi.org/10.1002/9781119625728, 2022.

Topping, D., Barley, M., Bane, M. K., Higham, N., Aumont, B., Dingle, N., and McFiggans, G.: UManSysProp v1.0: an online

and open-source facility for molecular property prediction and atmospheric aerosol calculations, Geosci. Model Dev., 9, 899–914, https://doi.org/10.5194/gmd-9-899-2016, 2016.

Topping, D., Connolly, P., and Reid, J.: PyBOX: An automated box-model generator for atmospheric chemistry and aerosol simulations, J. Open Source Software, 3, 28, https://doi.org/10.21105/joss.00755, 2018.

Valorso, R., Aumont, B., Camredon, M., Raventos-Duran, T., Mouchel-Vallon, C., Ng, N. L., Seinfeld, J. H., Lee-Taylor, J., and Madronich, S.: Explicit modelling of SOA formation from α-pinene photooxidation: sensitivity to vapour pressure estimation, Atmos. Chem. Phys., 11, 6895–6910, https://doi.org/10.5194/acp-11-6895-2011, 2011.

Wang, J., Shilling, J. E., Liu, J., Zelenyuk, A., Bell, D. M., Petters, M. D., Thalman, R., Mei, F., Zaveri, R. A., and Zheng, G.: Cloud droplet activation of secondary organic aerosol is mainly controlled by molecular weight, not water solubility, Atmos. Chem. Phys., 19, 941–954, https://doi.org/10.5194/acp-19-941-2019, 2019.

Xia, A. G., Michelangeli, D. V., and Makar, P. A.: Box model studies of the secondary organic aerosol formation under different HC/NO_x conditions using the subset of the Master Chemical Mechanism for α-pinene oxidation, J. Geophys. Res., 113, D10301, https://doi.org/10.1029/2007JD008726, 2008.

Xia, Z., Zhao, C., Yang, Z., Du, Q., Feng, J., Jin, C., Shi, J., and An, H.: Toward a learnable Artificial Intelligence Model for Aerosol Chemistry and Interactions (AIMACI) based on the Multi-Head Self-Attention algorithm, Atmos. Chem. Phys., 25, 6197–6218, https://doi.org/10.5194/acp-25-6197-2025, 2025.

Xu, J. L.: Simulated impact of NO_x on SOA formation from oxidation of toluene and m-xylene, MS thesis, Rice University, USA, ProQuest Number: 1602117, 2014.

Xu, S. X.: Investigating the role of highly oxygenated molecules (HOM) in aerosol using a newly developed box model PyCHAM, PhD thesis, University of Manchester, UK, ProQuest Number: 30731655, 2021.

Yu, F. and Luo, G.: Simulation of particle size distribution with a global aerosol model: contribution of nucleation to aerosol and CCN number concentrations, Atmos. Chem. Phys., 9, 7691–7710, https://doi.org/10.5194/acp-9-7691-2009, 2009.

Zaveri, R., Easter, R., Fast, J., and Peters, L.: Model for Simulating Aerosol Interactions and Chemistry (MOSAIC), J. Geophys. Res., 113, D13204, https://doi.org/10.1029/2007JD008782, 2008.

Zhang, C., Guo, Y., Shen, H., Luo, H., Pullinen, I., Schmitt, S. H., Wang, M., Fuchs, H., Kiendler-Scharr, A., Wahner, A., Mentel, T. F., and Zhao, D.: Contrasting influence of nitrogen oxides on the cloud condensation nuclei activity of monoterpene-derived secondary organic aerosol in daytime and nighttime oxidation, Geophys. Res. Lett., 50, e2022GL102110, https://doi.org/10.1029/2022GL102110, 2023.

Zhang, X., Cappa, C. D., Jathar, S. H., McVay, R. C., Ensberg, J. J., Kleeman, M. J., and Seinfeld, J. H.: Influence of vapor wall loss in laboratory chambers on yields of secondary organic aerosol, Proc. Natl. Acad. Sci. U.S.A., 111, 5802–5807, https://doi.org/10.1073/pnas.1404727111, 2014.

Zhao, D. F., Buchholz, A., Kortner, B., Schlag, P., Rubach, F., Kiendler-Scharr, A., Tillmann, R., Wahner, A., Flores, J. M., Rudich, Y., Watne, Å. K., Hallquist, M., Wildt, J., and Mentel, T. F.: Size-dependent hygroscopicity parameter (κ) and chemical composition of secondary organic cloud condensation nuclei, Geophys. Res. Lett., 42, 10920–10928, https://doi.org/10.1002/2015GL066497, 2015.

Zhao, D. F., Buchholz, A., Kortner, B., Schlag, P., Rubach, F., Fuchs, H., Kiendler-Scharr, A., Tillmann, R., Wahner, A., Watne, Å. K., Hallquist, M., Flores, J. M., Rudich, Y., Kristensen, K., Hansen, A. M. K., Glasius, M., Kourtchev, I., Kalberer, M., and Mentel, Th. F.: Cloud condensation nuclei activity, droplet growth kinetics, and hygroscopicity of biogenic and anthropogenic secondary organic aerosol (SOA), Atmos. Chem. Phys., 16, 1105–1121, https://doi.org/10.5194/acp-16-1105-2016, 2016.

Zhao, J., Häkkinen, E., Graeffe, F., Krechmer, J. E., Canagaratna, M. R., Worsnop, D. R., Kangasluoma, J., and Ehn, M.: A combined gas- and particle-phase analysis of highly oxygenated organic molecules (HOMs) from α-pinene ozonolysis, Atmos. Chem. Phys., 23, 3707–3730, https://doi.org/10.5194/acp-23-3707-2023, 2023.

Zuend, A. and Seinfeld, J. H.: Modeling the gas-particle partitioning of secondary organic aerosol: the importance of liquid-liquid phase separation, Atmos. Chem. Phys., 12, 3857–3882, https://doi.org/10.5194/acp-12-3857-2012, 2012.